Oxygen order–disorder phase transition in layered GdBaCo$_2$O$_{5+\delta}$ perovskite: Thermodynamic and transport properties

Liliana Mogni [a,*], Fernando Prado [b], Catalina Jiménez [c], Alberto Caneiro [a]

[a] CNEA-CONICET, Centro Atómico Bariloche, Av. Bustillo 9500, S.C. de Bariloche, Argentina
[b] CONICET, Universidad Nacional de Sur, Av. Alem, Bahia Blanca, Argentina
[c] Helmholtz Centre Berlin, Hahn-Meitner-Platz 1, D-14109 Berlin, Germany

ABSTRACT

The effects of the orthorhombic (O) to tetragonal (T) phase transition around 450/500 °C on the thermodynamic and transport properties of the layered cobaltite GdBaCo$_2$O$_{5+\delta}$ have been investigated in detail using complementary techniques such as thermo-gravimetry (TG), differential scanning calorimetry (DSC), dilatometry, angle dispersive as well as energy dispersive high temperature X-ray diffraction (HT-XRD and ED-XRD). Experimental data show that the O/T transition temperature shifts to higher values when the pO$_2$ of the experiment increases. The equilibrium pO$_2$ data shows the presence of a narrow two-phase field around $5 + \delta \approx 5.42$. The presence of a two-phase field together with an enthalpy change ($\Delta H \approx 4$ J/g) and HT-XRD data showing coexistence of both phases confirms that this phase transition is first-order type. Oxygen partial molar enthalpy and entropy of both phases, the "ordered" O and the "disordered" T, are obtained from TG under controlled pO$_2$, and yield lower entropy and enthalpy values for the ordered O phase. The O/T phase transition at constant temperature involves a volume contraction and a density change of 0.3%. Isotherms of electrical conductivity as a function of pO$_2$ show that this compound exhibits itinerant charge carrier behavior regardless of the crystal symmetry. The charge carrier mobility decreases for the T phase, which might be due to the shortening of Co−O−Co distance along a-direction.

© 2013 Elsevier B.V. All rights reserved.

1. Introduction

The family of compounds LnBaCo$_2$O$_{5+\delta}$ (Ln = lanthanide) has attracted great attention due to their remarkable magnetic and transport properties. These materials present spin-state transition [1–4], charge ordering [5,6], and giant magnetoresistance with resistivity ratios of $\approx 30\%$ [3,7]. These oxides also exhibit high oxygen surface exchange [8] and diffusivity [9] rates, which, combined with their high electrical conductivity [10–12], make them suitable for high temperature electrochemical devices, such as oxygen separation membranes [9,10,13] and solid oxide fuel cells (SOFC) [10,14].

The unit cell of LnBaCo$_2$O$_{5+\delta}$ has been reported to be orthorhombic of dimensions $a_p \times 2a_p \times 2a_p$ or $a_p \times a_p \times 2a_p$ (space group Pmmm), or tetragonal, of dimensions $a_p \times a_p \times 2a_p$ (S.G. P4/mmm) [2,15–18], where a_p refers to the lattice parameter of the primitive cubic perovskite. The symmetry and unit cell size depend on the oxygen content, temperature and on the Ln ionic size (see Fig. 1). The doubling of a_p along the c-axis is due to the location of Ln and Ba cations in alternative

layers perpendicular to the c-axis; while the cell doubling along the b-axis has been explained considering the ordering of the oxygen vacancies along the a-direction [2,19]. The orthorhombic symmetry appears when the oxygen content is $5 + \delta \approx 5.5$ and the thermal energy is not enough to produce a random distribution of the oxygen vacancies. In this case, the occupancy of the O(3) crystal site, located at (0, 1/2, 1/2), is close to 100%, while it is close to 0% for the O(4) crystal sites, located at (0, 0, 1/2). On the other hand, when the oxygen content is very different from 5.5, or the thermal energy is high enough to let the oxygen atoms occupy the O(4) crystal sites, the crystal structure becomes tetragonal with the LnO layers partially empty (see Fig. 1).

Taskin et al. [20] have suggested that the cationic ordering in the crystal structure reduces the oxygen bond strength leading to disorder-free pathways for oxygen ion diffusion, which are responsible for the higher rates observed in the ordered GdBaMn$_2$O$_{5+\delta}$, compared to the disordered Gd$_{0.5}$Ba$_{0.5}$MnO$_{3-x}$ phase. In addition, as the oxygen vacancies are located preferentially in the LnOx layers, it is possible to have Co−O−Co paths even at high temperature. Like other perovskite related oxides, the electronic conduction in LnBaCo$_2$O$_{5+\delta}$ occurs via an electron hopping mechanism along the Co−O−Co bonds through a double exchange process [10]. Then, the presence of linked Co−O−Co paths allows the achievement of high electrical conductivity values at high temperatures. The electrical conductivity also depends

* Corresponding author at: Centro Atómico Bariloche, 8400 S.C. de Bariloche, Argentina.
Tel.: +54 294 4445288; fax: +54 294 4445299.
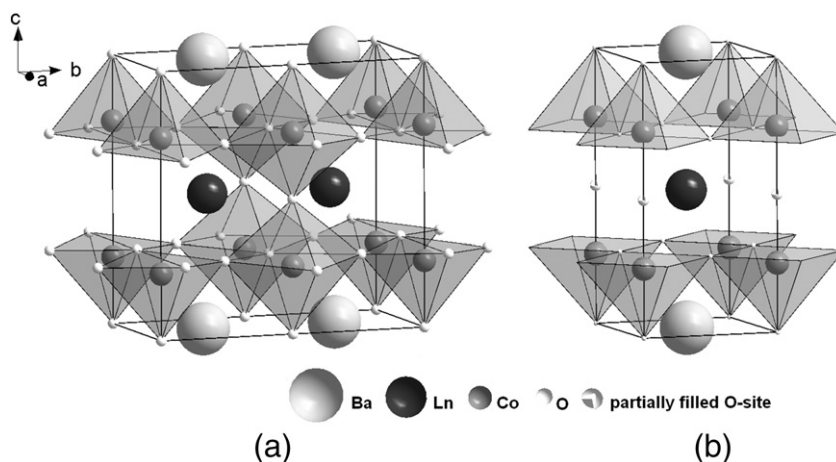*E-mail address:* mogni@cab.cnea.gov.ar (L. Mogni).

Fig. 1. Crystal structures of layered perovskites $LnBaCo_2O_{5+\delta}$ (Ln = lantanide). a) Orthorhombic and b) tetragonal phase.

on the oxygen content, temperature and rare earth size. These parameters affect the valence of the Co ions, and the angle and strength of the Co–O–Co bond and therefore the electrical conductivity [10,11].

Recent studies showed that $GdBaCo_2O_{5+\delta}$ is a potential candidate for high temperature ceramic devices because of their good high temperature properties. This oxide exhibits high oxygen surface exchange coefficient and oxygen diffusivity coefficients [8,12], good oxygen ionic conductivity ($\sigma_{ion} \approx 0.01$ S cm^{-1}) [12,20], and high electronic conductivity ($\sigma_{el} \approx 500$ S cm^{-1}) [21]. Besides, recent studies have reported low polarization resistances (Rp ≈ 0.15 Ω cm^2 at 750 °C [22], Rp ≈ 0.25 Ω cm^2 at 625 °C [8] and Rp ≈ 0.40 Ω cm^2 at 600 °C [23,24]) and achieve good power density values between 150 and 500 mW cm^{-2} in the range of 700–800 °C for $GdBaCo_2O_{5+\delta}$–LSGM/ LSGM/LDC/Ni-GDC [11,25] and $GdBaCo_2O_{5+\delta}$/YSZ/Ni-YSZ [26] cells.

Despite these promising properties, the performance of this oxide as SOFC-cathode or oxygen permeation membranes could be affected by the presence of an order–disorder phase transition taking place at around 500 °C [21]. This phase transition involves the rearrangement of the oxygen vacancies, and causes the transformation from the low-temperature orthorhombic phase (S.G. P*mmm*) to the high-temperature tetragonal phase (S.G. P4/*mmm*) [21]. This order–disorder transition is similar to that reported by Streule et al. [15,27] for $PrBaCo_2O_{5.48}$ at 503 °C. In addition, Tarancón et al. [21] reported that, across this phase transition, the electrochemical performance is not affected because of the high electrical conductivity values for both phases along with the monotonic change of unit cell volume through transition. However, the oxygen rearrangement across the phase transition modifies the oxygen ion pathways in the LnOx layers as well as the Co–O–Co bonds, likely affecting the mixed conductivity properties of these layered perovskites.

In this work we have carried out a systematic study of the thermodynamic and transport properties through the O/T transition in the double perovskite $GdBaCo_2O_{5+\delta}$. The experimental data obtained using complementary experimental techniques, allowed us to understand the feature of the O/T transition as well as the mechanism for the electrical conductivity at high temperature.

2. Experimental

$GdBaCo_2O_{5+\delta}$ was obtained by solid state reaction using Gd_2O_3, $BaCO_3$ and Co_3O_4 analytical grades as starting materials. These precursor materials were ball-milled for 30 min at 500 rpm using an agate container and subsequently heat treated in air at 1100 °C for 6 h applying heating and cooling rates of 3 °C/min. The presence of a single-orthorhombic phase was checked by room temperature XRD using a Philips PW1700 diffractometer with CuKα radiation

and a graphite monochromator. The crystal structures of the samples were analyzed by the Rietveld method using the FullProf Program [28].

Afterwards, an Anton Paar chamber was coupled to the same diffractometer in order to conduct an angle dispersive high temperature XRD study (HT-XRD) from room temperature to 900 °C and within $2\theta = 20$–80° under stationary air. Additionally, an electrochemical gas blending system consisting of a zirconia pump and oxygen sensor [29], to control and measure the pO$_2$ using He as gas carrier, was coupled for a thermodiffraction study between 400 and 500 °C and $10^{-5} \leq$ pO$_2 \leq 1$ atm.

Energy-dispersive X-ray diffraction (ED-XRD) of white synchrotron radiation in transmission geometry was used to monitor the phase transitions at the EDDI experimental station at the BESSY II synchrotron light source of the Helmholtz Centre Berlin. The powder sample was mounted in an Anton Paar DHS 1100 furnace equipped with an X-ray-transparent graphite dome, and then it was illuminated by a white beam of X-rays while the energy of diffracted photons between 10 and 100 keV was measured at $2\theta = 8$° by a multichannel analyzing detector[30,31]. Two atmospheres were used: air and Ar flow. The temperature was increased from 30 to 325 °C at 100 °C/min, and from 325 to 700 °C at 10 °C/min. Data acquisition and temperature cycles were computer-controlled by the software package Spec [32]. Each spectrum was acquired every 12.5 s; thus the temperature resolution for heating at 10 °C/min was 2.1 °C.

The thermal behavior was studied by DSC with a Modulated DSC 2910 TA Instruments at heating rates of 1 °C/min and 10 °C/min between room temperature and 550 °C under air and Ar atmospheres (110 ml/min).

Dense samples of $GdBaCo_2O_{5+\delta}$ were obtained by pressing the powder under a uniaxial pressure of 100 kg/m^2 followed by a heat treatment at 1200 °C for 6 h in air (see Fig. 2). The lattice expansion of these samples was determined from dilatometric measurements under air and O$_2$ atmospheres with two heating–cooling rates, 1 and 10 °C/min, between room temperature and 900 °C using a vertical Dilatometer LINSEIS L75VS1000C.

Resistivity measurements on the same dense samples were carried out by the four-probe techniques with a scanner-multimeter Agilent 3497A. The resistivity cell allows controlling temperature and pO$_2$ by means of a furnace coupled to the gas blending system described before. Resistivity (ρ) isotherms were collected while varying pO$_2$ between 10^{-4} and 1 atm for temperatures ranging from 380 to 900 °C. Conductivity data are obtained from the relation $\sigma = \rho^{-1}$.

Thermogravimetry under controlled atmospheres was performed using a symmetrical thermobalance based on a Cahn 1000 electrobalance coupled to the electrochemical gas blending system [29].
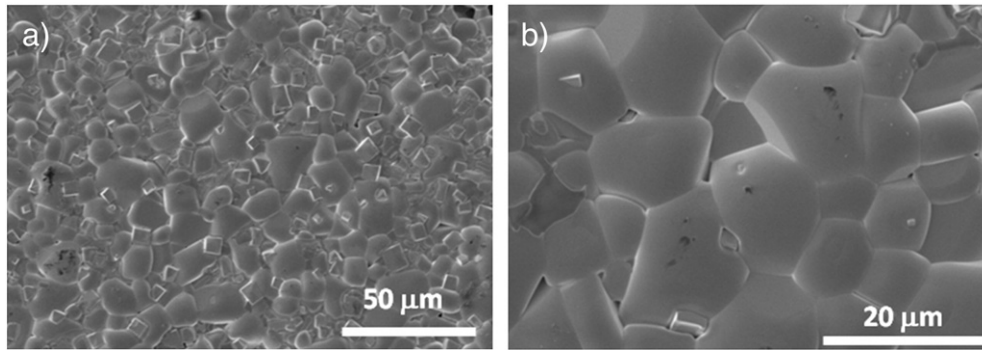
Fig. 2. FEG-SEM micrograph of GdBaCo$_2$O$_{5+\delta}$ dense sample sintered at 1200 °C by 6 h.

Dynamic measurements were carried out under air and Ar with heating–cooling rates of 10 °C/min between room temperature and 600 °C. Additionally, thermogravimetric measurements of the equilibrium pO$_2$ as a function of the oxygen content ($5 + \delta$) at constant temperature were performed between 380 and 900 °C. The accuracy of the thermobalance is ± 10 μg, i.e. it allows for the determination of ($5 + \delta$) variations of ± 0.0003 for 1 g of sample. The equilibrium criterion for the thermodynamic measurements was the constant sample weight with time. This equilibrium criterion was verified over a period of 24 h for the low T and pO$_2$ range of measurements. The absolute oxygen content of the samples was determined after performing the thermogravimetric measurements by reduction in dry H$_2$ at 1000 °C assuming BaO, Gd$_2$O$_3$ and Co as final products. These final products were confirmed by XRD.

3. Results and discussion

3.1. Temperature and atmosphere effect on O/T transition

Fig. 3a shows the X-ray diffraction data obtained in air at 20, 200, 400, 500, 700 and 900 °C for GdBaCo$_2$O$_{5+\delta}$. The O/T phase transition is clearly detected in the angle range $57 \leq 2\theta \leq 60^\circ$ between 450 and 500 °C (see Fig. 3b) where the reflections (142) and (222) of the ortho-rhombic phase merge into the reflection (212) of the tetragonal phase

indicating the crystal structure transformation. ED-XRD experiments were carried out to determine the O/T transition temperature (T$_{O/T}$) precisely. Fig. 4 shows the energy dispersive map as a function of T between 400 and 600 °C under air and Ar atmospheres. In the energy range between 44 and 48 keV the O/T phase transition can be monitored through the evolution of reflections (200) and (040) of the orthorhombic phase which join together at the transition temperature into the reflection (200) of the tetragonal phase. The experimental data indicate that, on heating, the O/T transition takes place at 480 ± 2 °C in air and at 429 ± 2 °C in Ar atmosphere.

In Fig. 5 the variations of the lattice parameters (a, b and c) and the unit cell volume are plotted as a function of T, between 20 and 900 °C. These data were obtained using the Rietveld method and crystallographic information reported by Frontera et al. [33] for the isostructural PrBaCo$_2$O$_{5 + \delta}$ compound. For better assessment all the values are referred to the primitive cubic perovskite cell parameters a_p (≈ 3.9 Å). Thus, for the orthorhombic Pmmm phase $a \approx a_p$, $b \approx 2a_p$ and $c \approx 2a_p$ while for the tetragonal structure $a = b \approx a_p$, and $c \approx 2a_p$. At 80 °C, the lattice parameters of the O phase exhibit a discontinuity associated to the low temperature insulator–metal transition reported in previous works by other authors [4,16,18] (in this case we used O$_I$ and O$_{II}$ for insulator and metallic phases, respectively; both with orthorhombic symmetry). As the temperature increases the lattice parameters a and b of the O phase converge to the same value around
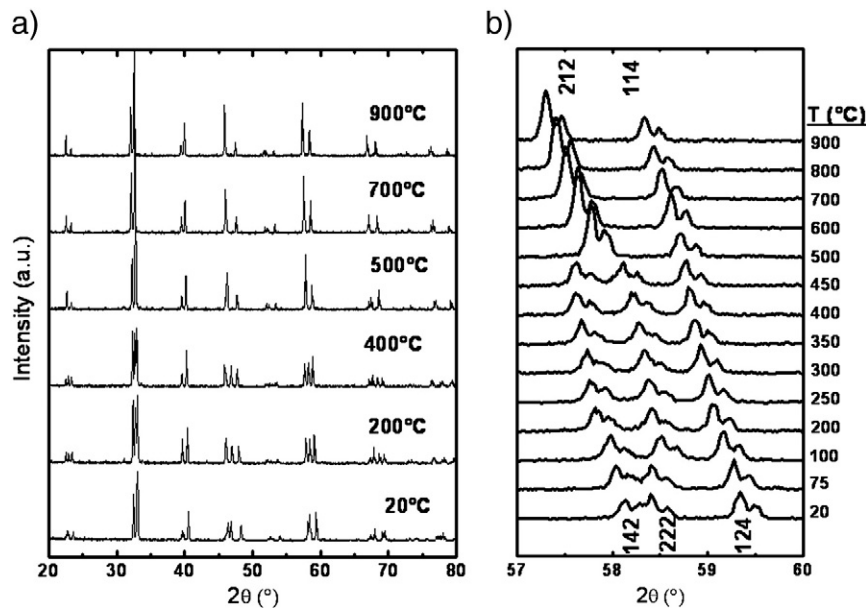

Fig. 3. a) Representative XRD patterns of GdBaCo$_2$O$_{5+\delta}$ as a function of T in air between 20 and 900 °C. b) Splitting of the reflection (212) of the tetragonal phase into reflections (142) and (222) of the orthorhombic phase.
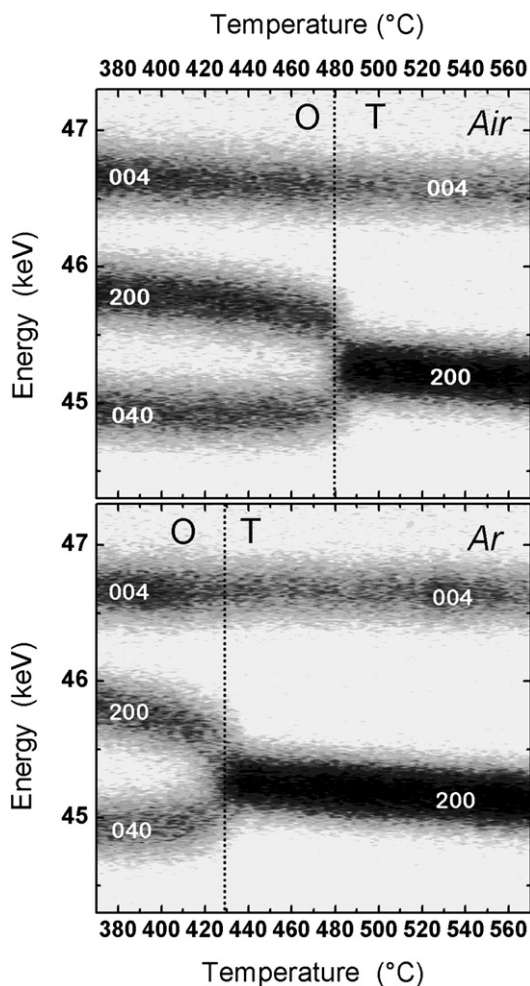
Fig. 4. Energy dispersive map of diffraction intensities (dark-gray is high intensity) vs. temperature obtained by ED-XRD a) in air and b) under flowing Ar. The characteristic merging of the 200 and 040 diffraction lines of the orthorhombic phase (O) into the 200 line of the tetragonal one (T) is observed.

Fig. 5. a) Lattice parameters and b) unit cell volume as a function of T obtained by HT-XRD and ED-XRD in air. The values are related to a_p.

450–500 °C, which indicates the O/T phase transition. The lattice parameters and the phase transition temperature ($T_{OI/OII} \approx 80$ °C and $T_{OII/T} \approx 481$ °C) are comparable to those previously reported in literature [6,21]. Fig. 5 also includes the lattice parameters calculated from ED-XRD data. A good agreement is observed between ED-XRD and HT-XRD techniques, even at the transition temperature. The variation of the unit cell volume as a function of temperature is shown in Fig. 5b. At the O/T transition temperature the unit cell volume shows no discontinuity suggesting that, if it exists, the volume change should be negligible compared with the variation of the total expansion with T.

Linear expansion measurements were carried out to evaluate the thermal expansion coefficients (TECs) of GdBaCo$_2$O$_{5+\delta}$. Fig. 6a shows the $\Delta L/L_0$ vs. T curves, where ΔL is the length change and L_0 is the initial length of the sample at 20 °C. These measurements were carried out using heating–cooling rates of 1 °C/min under air and O$_2$ atmospheres. For comparison, linear expansion data obtained from HT-XRD in air is also plotted in Fig. 6a considering $L = V_{u.c.}^{1/3}$. Table 1 shows the expansion coefficient values $\alpha = \dfrac{\Delta L/L_0}{\Delta T}$ obtained from dilatometry and HT-XRD in air. These values were obtained from the temperature range before the O/T transition, $20 \leq T \leq 450$ °C, after the O/T transition, $500 \leq T \leq 900$ °C, and for the whole temperature range, $20 \leq T \leq 900$ °C. These values are slightly lower than those recently reported by Liu et al. [34] (21.4×10^{-6} K^{-1} between 500 and
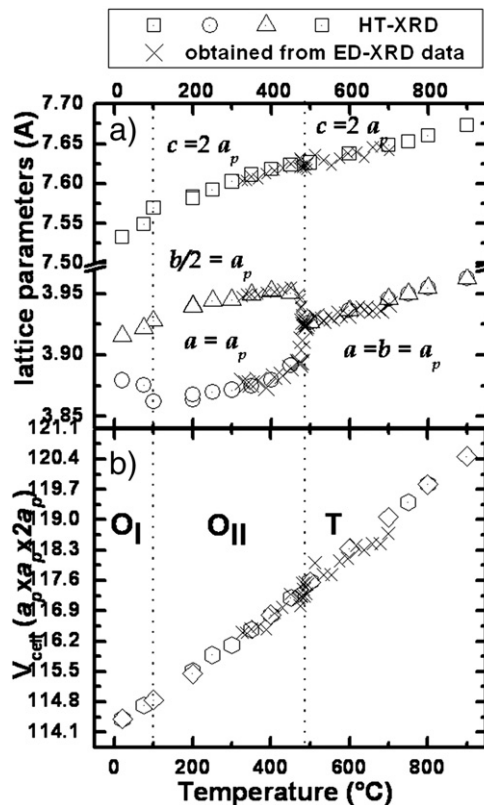
900 °C) and Wei et al. [24] (20.0×10^{-6} K^{-1} between 30 and 900 °C) but they are similar to the value reported by Tarancón et al. [21] (16.4×10^{-6} K^{-1} between 20 and 700 °C). Fig. 6b and c shows the d($\Delta L/L_0$)/dT vs. T curves between 400 and 550 °C for the plots obtained under pure O$_2$ and air, respectively. The presence of the O/T phase transition is clearly observed as a discontinuity, which shifts to lower temperature as the atmosphere becomes more reducing. Thus, when heated under O$_2$, the phase transition temperature was determined at $T_{O/T} = 493$ °C, while in air was $T_{O/T} = 472$ °C. In addition, hysteresis of 5–6 °C between the heating and cooling runs was detected at the O/T transition.

The heat flow as a function of temperature was determined by DSC measurements under flowing air and Ar. Two characteristic peaks were detected (see Fig. 7). The first peak at 80 °C corresponds to the insulator/metal transition reported for the orthorhombic phase [4,16,18], it seems to be independent of the atmosphere. As observed in Fig. 3 both, metal and insulator phases (O$_I$ and O$_{II}$), could be indexed with orthorhombic symmetry. The second peak, between 400 and 500 °C, is associated to the O/T phase transition. The $T_{O/T}$ values obtained from DSC measurements under air and Ar were 473 and 448 °C, respectively, while the enthalpy change was $\Delta H_{O/T} \approx 4$ J/g, which indicates a first order phase transition.

The variation of $T_{O/T}$ with the atmosphere in calorimetric, dilatation and energy dispersion experiment would indicate that this transition in GdBaCo$_2$O$_{5+\delta}$ depends not only on temperature but also on the oxygen content. The dependence of this transition with T has been previously reported by Streule et al. [27] for the isostructural compound PrBaCo$_2$O$_{5+\delta}$. In this study, the authors fixed the oxygen content in $5 + \delta = 5.48$ and observed the O/T transition by neutron powder diffraction (NPD) at 503 °C [27]. On the other hand, the effect of the oxygen content on the structure of PrBaCo$_2$O$_{5+\delta}$ has also been studied by NPD at room temperature using samples with controlled
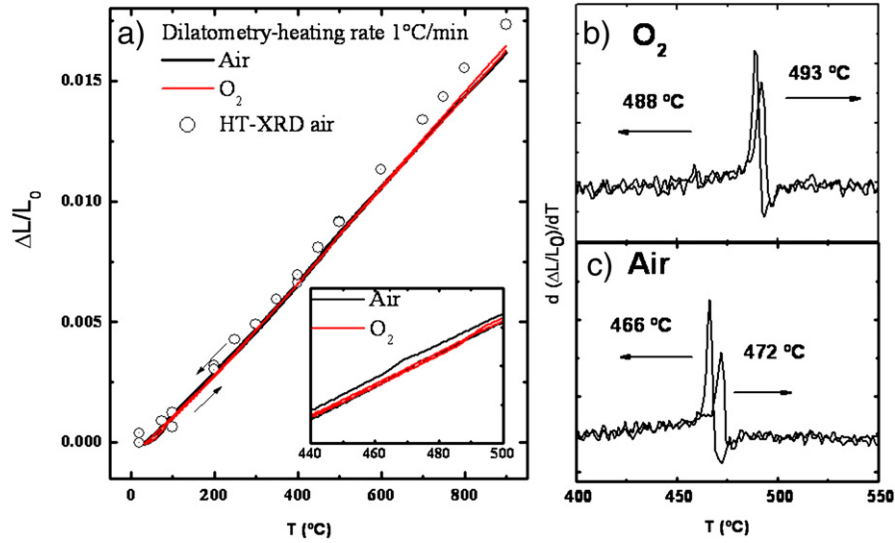
Fig. 6. a) $\Delta L/L_0$ vs. T curves obtained by dilatometry and HT-XRD ($L_{\text{HT-XRD}} = V_{u.c.}^{1/3}$) in air and O_2 atmospheres. The variations of the derivative $d(\Delta L/L_0)/dT$ with temperature under O_2 and air are shown in b and c, respectively.

oxygen content. In this case, the symmetry of the crystal structure varies from tetragonal P4/*mmm* for PrBaCo$_2$O$_{5.74}$ to orthorhombic P*mmm* for PrBaCo$_2$O$_{5.50}$ and finally to tetragonal P4/*mmm* again for PrBaCo$_2$O$_{5.176}$ [33]. In the case of the other related compound, NdBaCo$_2$O$_{5 + \delta}$, independent NPD studies for samples with controlled oxygen content gave contradictory results. While Burley et al. [17] have always found orthorhombic symmetry for samples with different oxygen contents, Anderson et al. [35] observed that the crystal structure transforms, first from tetragonal ($5 + \delta \geq 5.6$) to orthorhombic ($5.6 \geq 5 + \delta \geq 5.4$) and then back to tetragonal ($5.4 \geq 5 + \delta$) when the oxygen content is modified. These results suggest a combined effect of temperature and oxygen vacancy concentration on the order/disorder transition observed in the LnBaCo$_2$O$_{5 + \delta}$ compounds.

Aiming to clarify these results, a thermogravimetric study was carried out under air and Ar atmospheres in order to obtain a direct correlation between oxygen content and the O/T transition temperature for GdBaCo$_2$O$_{5+\delta}$ (see Fig. 8a). The curve obtained under air clearly shows the O/T transition between 450 and 500 °C together with hysteresis between the heating and the cooling runs. In contrast, the O/T transition results less evident in the case of the data obtained under Ar. However, the derivative of the oxygen content curve with respect to the temperature (Fig. 8b and c) reveals the presence of the O/T phase transition. During the cooling process in Ar, the O/T transition cannot be observed due to the impossibility of the sample to uptake oxygen from the atmosphere. Increasing T, the T$_{O/T}$ changes from 485 °C in air to 465 °C in Ar. Oxygen content varies from 5.44 to 5.46 across the phase transition in air and from 5.43 to 5.44 in Ar suggesting the presence of a narrow two-phase field in the temperature–oxygen content phase diagram of GdBaCo$_2$O$_{5+\delta}$.

Table 2 presents the T$_{O/T}$ values obtained in this work under O$_2$, air, and Ar. Differences in the T$_{O/T}$ values determined from different techniques under the same atmosphere may be related to the

experimental setup or variations in the heating rate. Phase transitions are traditionally classified by the singular behavior of the derivatives of the Gibbs potential. If some of these derivatives are discontinuous, the phase transition is of first-order. In this case, a latent heat is involved during transition and therefore the temperature of the system will stay constant producing a "mixed-phase regime" in which some parts of the system have completed the transition and others have not (two-phase field). If all the first derivatives are continuous, but discontinuities (or worse singularities) appear in the second order derivatives, then we are dealing with a second order phase transition in which case a continuous phase transition is observed. Therefore, the results discussed in this section lead us to conclude that this structural order/disorder transition is a first-order phase transition, characterized by a small heat of transformation $\Delta H_{O/T} \approx 4$ J/g, a narrow two-phase field in the oxygen content range $5.43 \leq 5 + \delta \leq 5.46$ and hysteresis of about 5–10 °C.

3.2. Thermodynamic analysis

In the previous section we have studied the O/T transition using complementary techniques through dynamic measurements. In this
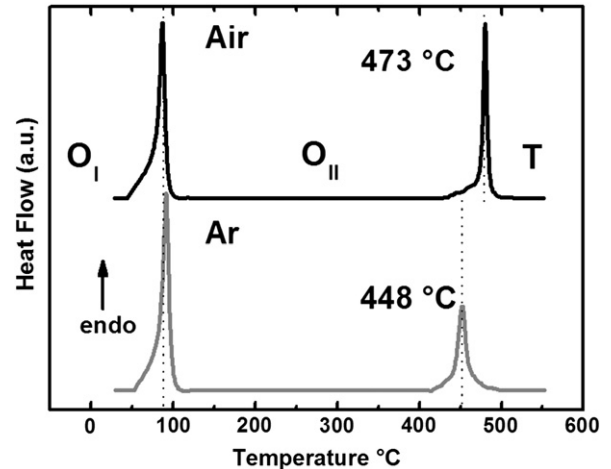
Table 1
Expansion coefficient values for GdBaCo$_2$O$_{5+\delta}$ obtained from dilatometry and HT-XRD in air.

	α (10^{-6} K^{-1})		
	20–450 °C	500–900 °C	20–900 °C
Dilatometry	17.6	19.0	18.4
HT-XRD	18.8	20.5	19.7

Fig. 7. Heat flow as a function of T obtained by DSC under air and Ar. Heating rate 10 °C/min.
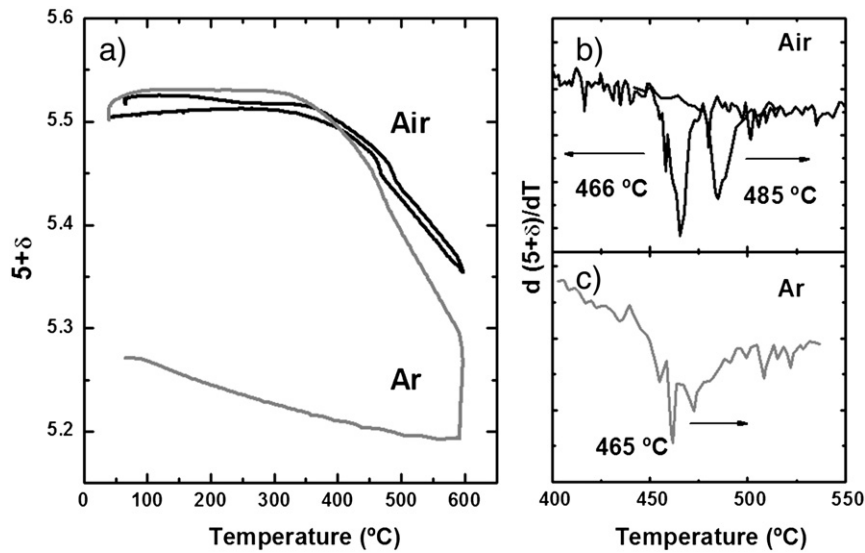
Fig. 8. a) Variation of oxygen content with T under air and Ar atmospheres with heating and cooling rate of 10 °C/min. The derivative of the oxygen content with respect to T obtained under b) air and c) Ar reveals the O/T phase transition.

section we studied the thermodynamic properties of GdBaCo$_2$O$_{5+\delta}$ by means of thermogravimetric measurements of the equilibrium pO$_2$. Fig. 9 shows the equilibrium oxygen partial pressure (pO$_2$) data as a function of oxygen content $(5 + \delta)$ obtained at constant temperature for values between 380 and 900 °C. Dotted lines are included as a guide indicating the O/T phase transition and the two-phase field. These results were confirmed by HT-XRD measurements at constant temperature with the pO$_2$ varying from 1 to 10^{-4} atm. Fig. 10a displays the XRD diffraction data at T = 440 °C at various pO$_2$. Fig. 10b magnifies the 2θ range between $56 < 2\theta < 60°$ where reflections (142) and (222) of the orthorhombic phase merge into the reflection (212) of the tetragonal phase due to the crystal structure transformation. Also, the XRD data obtained under pO$_2$ = 0.026 atm reveal the coexistence of the two phases (see Fig. 10b) in agreement with thermogravimetric data of the equilibrium pO$_2$ (Fig. 9). The oxygen content range where the two phases coexist is located around $5 + \delta = 5.42$ and the width of this region increases as T decreases. Finally, at the high temperature and low pO$_2$ range, isotherms converge to the stoichiometric compound GdBaCo$_2$O$_{5.50}$. These results are in good agreement with those recently reported by Tsevetkov et al. [36], who determined the defect structure of GdBaCo$_2$O$_{5+\delta}$ studied by coulometric measurements in the temperature and pO$_2$ ranges $900 \leq T \leq 1050$ °C and $10^{-6} \leq pO_2 \leq 1$ atm. Below pO$_2$ = 10^{-4} atm, these authors have found oxygen content values even lower than $5 + \delta = 5.00$ for $T \geq 900$ °C [36].

Fig. 11 shows the unit cell volume and lattice parameter changes as a function of $5 + \delta$. These results were obtained from the combination of thermogravimetric (Fig. 9) and XRD data measured at T = 440 °C varying the pO$_2$ (Fig. 10). Unlike the behavior observed for

the unit cell volume across the phase transition when temperature changes at constant pO$_2$ = 0.209 atm (see Fig. 5), at constant temperature and varying pO$_2$ the lattice parameters and unit cell volume show a discontinuity which is not observed in Fig. 5 because it may be masked by thermal expansion effect.

In thermodynamic equilibrium, the oxygen chemical potential of GdBaCo$_2$O$_{5+\delta}$ $\left(\mu_{O_2}\right)$ is related to the oxygen chemical potential of the gas phase $\left(\mu_{O_2}^{gas}\right)$ and then to the pO$_2$, by the relation [37–40]:

$$\mu_{O_2} = \mu_{O_2}^{gas} = \mu_{O_2}^0(T) + RT\ln\left(pO_2/pO_2^0\right) \tag{1}$$

where R is the gas constant, pO$_2^0$ = 1 atm and μ_{O2}^0 (T) is the oxygen chemical potential of the reference gas [41].

Besides, the oxygen partial molar enthalpy $\left(h_{O_2}\right)$ and entropy $\left(s_{O_2}\right)$ could be obtained from the relations:

$$h_{O_2} = \frac{\partial\left(\mu_{O_2}/T\right)}{\partial\left(1/T\right)}\bigg|_{5+\delta} \tag{2}$$

Table 2
Temperature orthorhombic/tetragonal phase transition (T$_{O/T}$) obtained by different techniques.

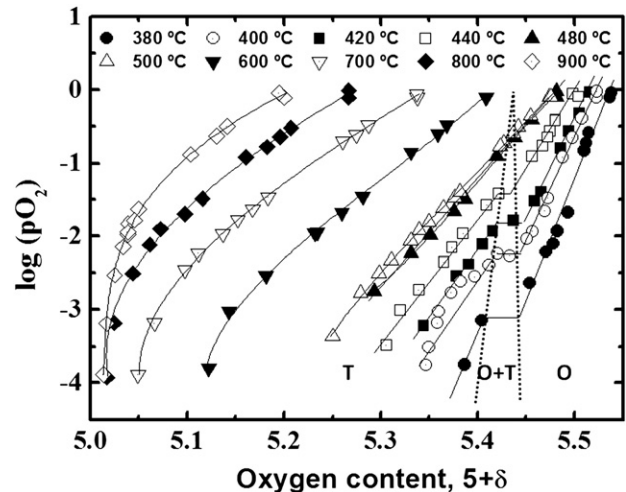|	T$_{O/T}$ (°C)[a]		
	O$_2$	Air	Ar
ED-XRD		481	430
Dilatometry	493	472	–
DSC	–	473	448
Thermogrametry	–	482	465

[a] Under heating condition.

Fig. 9. Variation of the oxygen content $(5 + \delta)$ with equilibrium pO$_2$ for GdBaCo$_2$O$_{5+\delta}$ as a function of temperature varying between 380 and 900 °C.

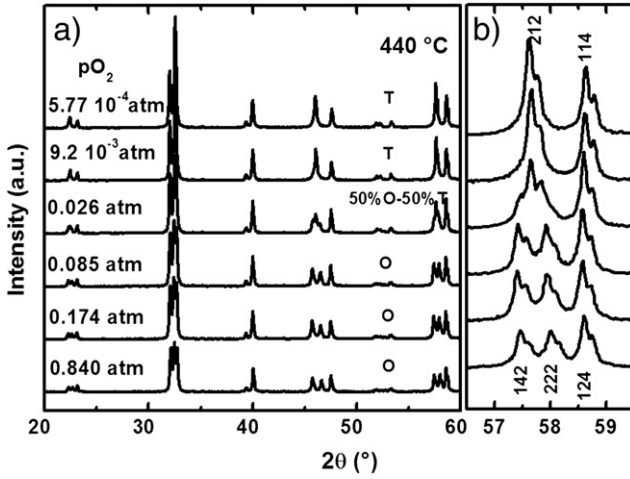**Fig. 10.** a) XRD patterns of GdBaCo$_2$O$_{5+\delta}$ as a function of pO$_2$ between 10^{-4} and 1 atm at 440 °C. b) Splitting of reflection (212) of the tetragonal phase into reflections (142) and (222) of the orthorhombic phase.

and

$$s_{O_2} = \left.\frac{\partial\left(\mu_{O_2}\right)}{\partial(T)}\right|_{5+\delta}.$$ (3)

Figs. 12a and 13a show some representatives $\left.\frac{\mu_{O_2}}{T}\right|_{5+\delta}$ vs. $^1/_T$ and $\left.\mu_{O_2}\right|_{5+\delta}$ vs. T curves, respectively, obtained for oxygen content value between $5.05 < 5 + \delta < 5.50$. The structural transformation is clearly revealed in Figs. 12a and 13a through the slope change in the $\left.\frac{\mu_{O_2}}{T}\right|_{5+\delta}$
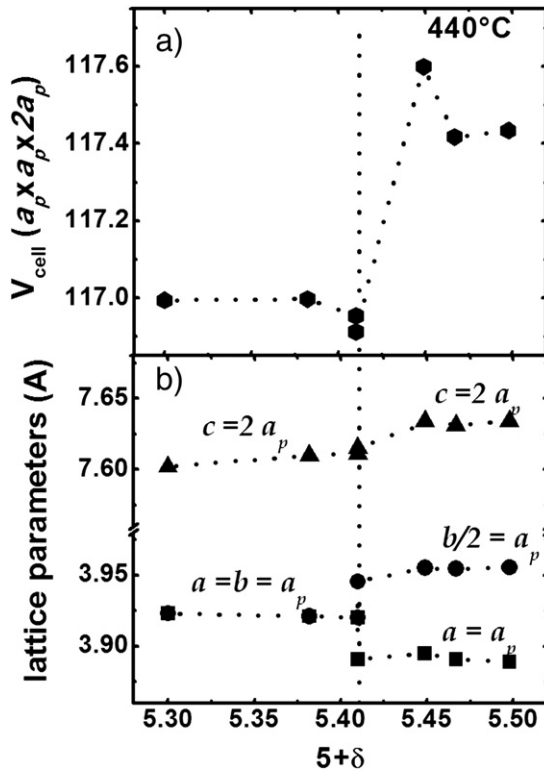

Fig. 11. a) Unit cell volume and b) lattice parameters as a function of the oxygen content $5 + \delta$, obtained combining XRD and thermogravimetric data at 440 °C between $10^{-4} < pO_2 < 1$ atm (see text). The values are related to a_p the lattice parameter of the primitive cubic perovskite.

vs. $^1/_T$ and $\mu_{O_2}|_{5+\delta}$ vs. T curves with noticeable differences in the partial molar properties (h$_{O_2}$ and s$_{O_2}$) for each phase (see Figs. 12b and 13b).

Recently, Tsevetkov et al. [36] have studied the defect structure of GdBaCo$_2$O$_{5+\delta}$ within the oxygen content range $4.85 \leq 5 + \delta \leq 5.15$. They found that h$_{O_2}$ and s$_{O_2}$ show a dramatic growth close to $5 + \delta = 5.00$. This behavior has been explained considering GdCoO$_3$ as a reference state, the presence of localized charges on the Co sites where Co^{+2}, Co^{+3} and Co^{+4} ions coexist and the formation of electrostatic clusters where oxygen vacancies are associated to Ba sites. Considering Kröguer–Vink notation the species reported by Tsevetkov et al. [36] coexisting close to $5 + \delta = 5.00$ are Gd$_{Gd}^x$,Ba$_{Gd}^{'}$,Co$_{Co}^x$,Co$_{Co}^{'}$,Co$_{Co}^{\cdot}$, V$_O^{\cdot\cdot}$,O$_O^x$ and $(V_O^{\cdot\cdot} - Ba_{Gd}^{'})^{\cdot}$.

In our case, the nearly linear dependence of h$_{O_2}$ with the oxygen content in the range $5.05 \leq 5 + \delta \leq 5.50$ is similar to that observed for other cobaltites with perovskite related structures [37–40,42–45]. In those cases, the presence of itinerant charge carriers in the Co3d–O2p band is assumed and the oxygen vacancy formation is described by the defect reaction:

$$\frac{1}{2}O_2 + V_O^{\cdot\cdot} + 2e' \rightleftharpoons O_O^x$$ (4)

where e' is an itinerating charge carrier in a partially filled wide Co3d–O2p band whose contribution to the partial molar properties is described by the Rigid Band Model (RBM) formalism considering [43–45]:

$$\mu_{e'} - \mu_{e'}^0(T) = \frac{n - n^0}{g(E_F)[Co]}$$ (5)

where n and n^0 indicate the electron occupation number in GdBaCo$_2$O$_{5+\delta}$ and the reference state, respectively, while $g(E_F)$ indicates the density of states at the Fermi level. The entropy of electrons is neglected considering that the electron band is very broad and is partially filled [42]. This picture of delocalized charge carriers is supported by the transport properties discussed in the next section considering that the predominant charge carriers are electron-hole occupation (p = 2–n).

The chemical potential of oxygen vacancies can be defined assuming the presence of point defects without interactions and randomly distributed in the oxygen lattice site:

$$\mu_V = \mu_{V_O^{\cdot\cdot}} - \mu_{O_O^x} = \mu_V^0(T) + RT\,ln\left(\frac{[V_O^{\cdot\cdot}]}{[O_O^x]}\right)$$ (6)

where $\mu_{V_O^{\cdot\cdot}}$ and $\mu_{O_O^x}$ are the chemical potential of oxygen vacancies and oxygen sites, defined as $\mu_{V_O^{\cdot\cdot}} = \mu_{V_O^{\cdot\cdot}}^0(T) + RT\,ln([V_O^{\cdot\cdot}])$ and $\mu_{O_O^x} = \mu_{O_O^x}^0(T) + RT\,ln([O_O^x])$, respectively. Therefore the reference chemical potential of vacancy formation is $\mu_V^0(T) = \mu_{V_O^{\cdot\cdot}}^0 - \mu_{O_O^x}^0$.

This expression is not necessarily valid for the orthorhombic phase, where some configurations are excluded due to the ordering of oxygen vacancies. However, Eq. (6) seems to be a good approximation for the tetragonal phase taking into account that not all oxygen lattice site contribute to oxygen vacancy formation.

In view of the defect reaction (4) and Eqs. (5) and (6), the following expression for h$_{O_2}$ and s$_{O_2}$ is obtained:

$$h_{O_2} = -2h_V^0 - h_e^0 - 4\frac{n - n^0}{g(E_F)[Co]}$$ (7)

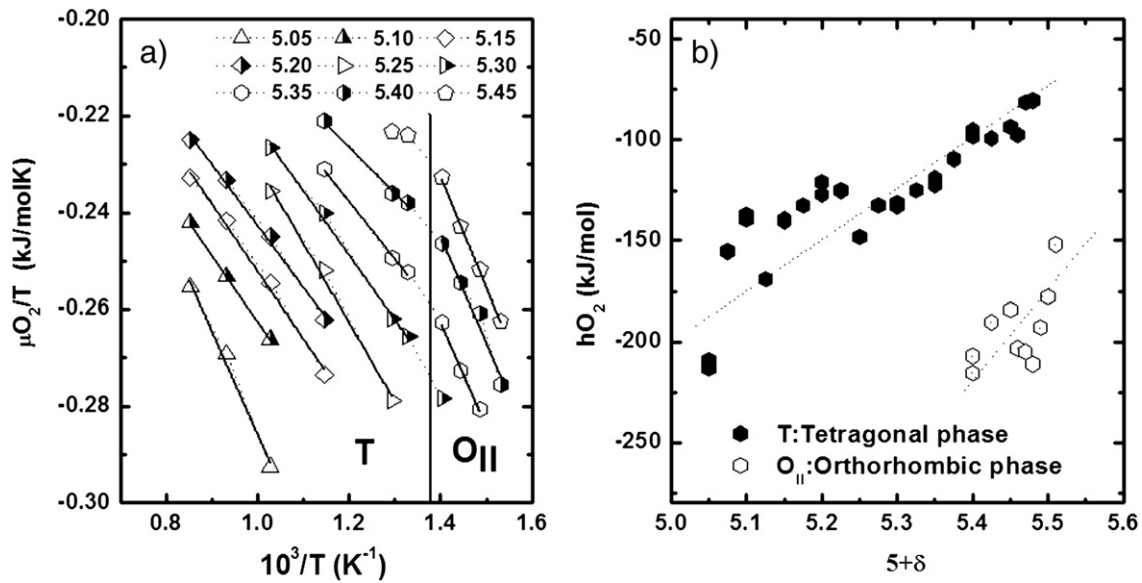$$s_{O_2} = -2s_V^0 - s_e^0 - 2R\,ln\left(\frac{[O_O^x]}{[V_O^{\cdot\cdot}]}\right).$$ (8)

Fig. 12. a) Representatives $\frac{\mu_{O_2}}{T}|_{5+\delta}$ vs. $1/T$ curves obtained from equilibrium pO$_2$ data for several oxygen contents $(5 + \delta)$. b) Partial molar enthalpy h_{O_2} as a function of $5 + \delta$ for both, orthorhombic and tetragonal phases.

Considering GdCoO$_3$ as a reference state, the charge neutrality condition, $n - n^0 = 2[V_O^{\cdot\cdot}] - [Ba_{Gd}'] = 2(1 - \delta) - 1$ and the mole fraction of Co sites [Co] = 2, the h_{O_2} vs $5 + \delta$ curve is fitted with Eq. (7) for the tetragonal phase (see Fig. 12b). The obtained values from fitting are $g(E_F) = 0.020(2)$ $(kJmol^{-1})^{-1}$ and $h_{O_2}^0 = -2h_{V_O}^0 - 4h_{e\ell}^0 = -83(6)$ kJmol^{-1}.

Fig. 12b also shows that the absolute h_{O_2} values for the orthorhombic phase are higher than those of the tetragonal phase. The higher h_{O_2} for the O phase should be related to a higher interaction between defects which predominates over the thermal energy leading to the ordering of the oxygen vacancies along the a-direction.

In Fig. 13b the variation of the partial molar entropy s_{O_2} as a function of $5 + \delta$ is shown. While s_{O_2} shows little dependence on the oxygen content for both phases, a great difference was observed between the values obtained for the oxygen ordered phase (O), $s_{O_2} \approx -50$ J mol^{-1} K^{-1}, and those obtained for the oxygen disordered phase (T) phase, $s_{O_2} \approx +100$ J mol^{-1} K^{-1}. The variation of s_{O_2} with $5 + \delta$ for the tetragonal phase is in agreement with the

defect Eq. (4) where delocalized charge carriers in Co−O band are proposed. The experimental data are fitted with Eq. (8) considering that the oxygen vacancies were randomly distributed in the oxygen sites located in the GdO$_x$ and CoO$_x$ layers. This assumption is in agreement with the ability of this compound to accommodate oxygen vacancies even at $5 + \delta \leq 5.00$ as reported by Tsevetkov et al. [36]. In the case of the orthorhombic phase it was impossible for us to fit the s_{O_2} vs $5 + \delta$ data since they are widely spread around a constant value. Despite this, the lower values of s_{O_2} for the orthorhombic phase compared to those of the tetragonal phase should be related to the ordering of the oxygen vacancies in the former. The ordering of oxygen vacancies reduces the number of possible configurations diminishing the configurational entropy [42].

3.3. Electron transport analysis

At high temperatures the GdBaCo$_2$O$_{5+\delta}$ is a mixed conductor with two contributions to the total conductivity (σ_T): the oxide ion and
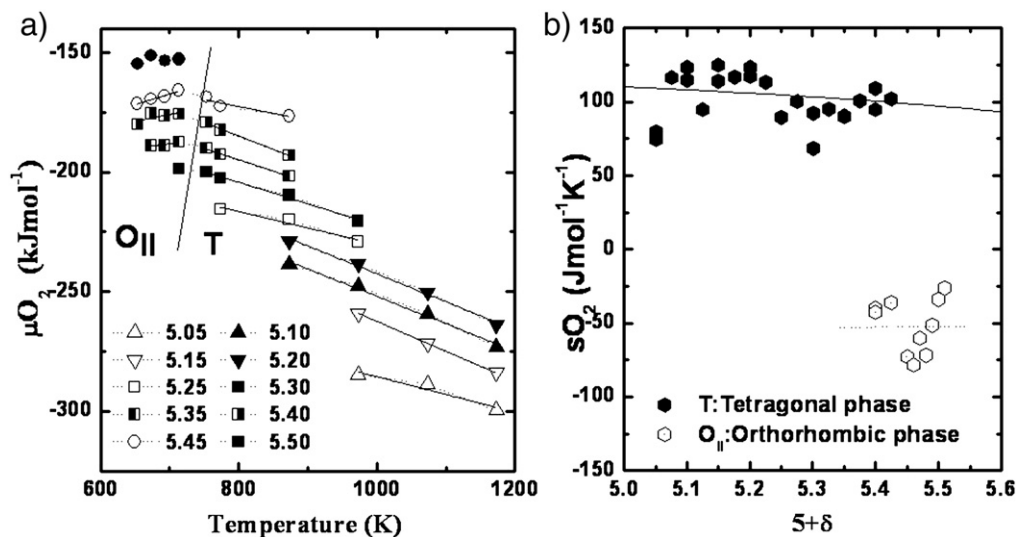

Fig. 13. a) Representatives $\mu_{O_2}|_{5+\delta}$ vs. T obtained from equilibrium pO$_2$ (see text) for several values of oxygen content $(5 + \delta)$. b) s_{O_2} as a function of $5 + \delta$ for both, orthorhombic and tetragonal phases.

electronic. Despite the high oxygen-vacancies concentration, the main contribution is due to electronic carriers since the electronic mobility is much higher than ionic one. Thus, for example Tsevetkov et al. [46] reported for $GdBaCo_2O_{5+\delta}$ oxygen vacancy mobilities about 8×10^{-6} cm^2 V^{-1} s^{-1} at 900 °C while the electron-hole mobilities reach values of 0.40 cm^2 V^{-1} s^{-1} at 870 °C. In this case the authors estimated the electron hole mobilities from a defect model with localized charge carriers [36]. This effect is also reflected in the relation between ionic conductivity ($\sigma_{ion} \approx 0.01$ S cm^{-1}) [12,20], and electronic conductivity ($\sigma_{el} \approx 500$ S cm^{-1}) [12,21]. Therefore, in our discussion we assume that $\sigma_T \approx \sigma_{el}$.

Fig. 14 shows the isothermal measurements of the electrical resistivity (ρ as a function of pO$_2$ for $GdBaCo_2O_{5+\delta}$). Measurements were carried out at various temperatures between 380 and 900 °C in the pO$_2$ range $10^{-4} \leq pO_2 \leq 1$ atm. The slopes of log(ρ) vs. log(pO$_2$) curves are negative, which is expected when p-type charge carriers predominate. Roughly, three regions for the experimental data can be distinguished: a) the region corresponding to the orthorhombic phase at low temperature and high pO$_2$ where electrical resistivity is almost independent of pO$_2$; b) the region at intermediate T and pO$_2$ values where the tetragonal phase is stable and the slopes of log (ρ) vs. log (pO$_2$) curves are larger than in the other regions and c) the region at high T and low pO$_2$, where the stabilization of the compound $GdBaCo_2O_{5.0}$ leads to a low-dependence of the electrical resistivity with pO$_2$. The behavior of ρ in those regions where it barely changes with pO$_2$ is related to the small variation of the oxygen vacancy concentration which is linked to the charge carrier concentration through balance charge condition. The behavior of ρ as a function of T and pO$_2$ for the tetragonal phase is similar to the experimental data reported by other authors for $GdBaCo_2O_{5+\delta}$ [12,46].

The variation of the electrical conductivity σ as a function of the oxygen content, $5 + \delta$, at constant temperature can be obtained combining the log (ρ) vs. log (pO$_2$) curves with thermogravimetric data of the equilibrium pO$_2$. In Fig. 15 the σ vs. $5 + \delta$ curves are plotted at several temperatures. In this figure it can be observed that, at constant oxygen content, the conductivity σ is almost independent with T. The nonthermal activated behavior and the high values of conductivity suggest a metallic-type mechanism which is consistent with the presence of delocalized charge carriers as predicted from thermodynamic properties. Like other perovskites with itinerant charge carriers and predominant p-type conductivity [45] the charge carrier concentration, c_p could be approximated by:

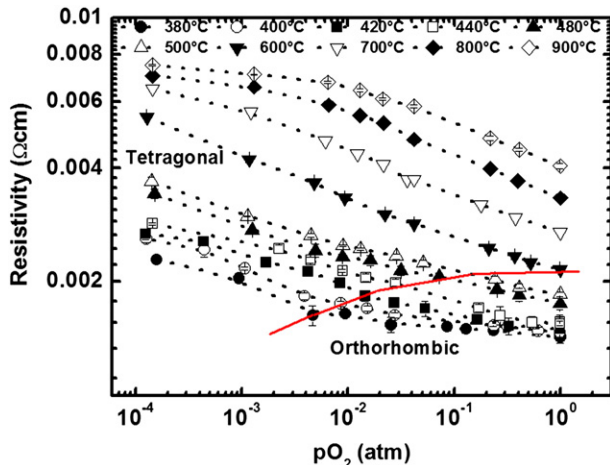$$c_p = \frac{2}{V_{u.c.}}(2-n) = \frac{2}{V_{u.c.}}\left(2-n^0 + 1 - 2(1-\delta)\right) \quad (9)$$

Fig. 14. ρ vs log pO$_2$ curves at constant temperature for T values between 380 and 900 °C. The red line indicates the O/T phase transition.

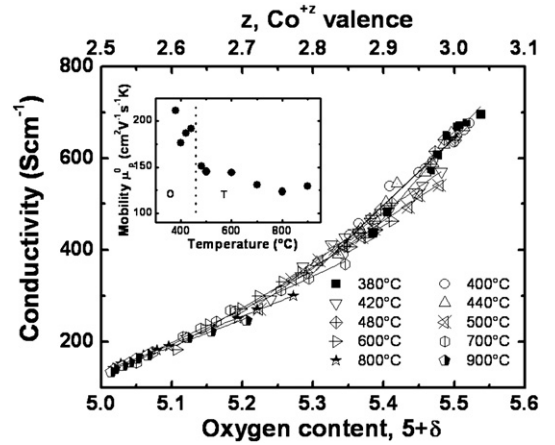**Fig. 15.** Electrical conductivity of $GdBaCo_2O_{5+\delta}$ as a function of the oxygen content $5 + \delta$. The inset shows the mobility values obtained from the σ vs. T curves.

where (p = 2–n) is the electron-hole occupation number into the band and the factor $\frac{2}{V_{u.c.}}$ is included considering two Co3d–O2p bands by unit cell volume in $GdBaCo_2O_{5+\delta}$.

Then the electronic conductivity can be approximated by:

$$\sigma = c_p e \mu_p = \frac{2}{V_{u.c.}}\left(2-n^0 + 1 - 2(1-\delta)\right)e\frac{\mu_p^0}{T} \quad (10)$$

where e is the electron charge and μ_p is the electron hole mobility. Considering $GdBaCo_2O_{5+\delta}$ exhibits a metallic behavior, the charge carrier mobility can be approached with the relation $\mu_p = \frac{\mu_p^0}{T}$. The values of the mobility μ_p^0 at a given temperature can be obtained by fitting the conductivity data in Fig. 15 using Eq. (7) and taking $V_{u.c.}$ from data plotted in Fig. 5b. The inset in Fig. 15 shows the variation of μ_p^0 with temperature through the O/T phase transition. As can be observed, μ_p^0 increases from 125 cm^2 V^{-1} s^{-1} K for the tetragonal phase to 200 cm^2 V^{-1} s^{-1} K for the orthorhombic phase. This effect may be due to the shortening in Co–O–Co bond along a-direction when the crystal structure transforms from tetragonal to orthorhombic. In both cases, the values obtained for $\frac{\mu_p^0}{T}$ are characteristic of large polaron electric transport mechanism where the free charge carriers move slowly because they must drag their polarization cloud through the polar solid.

4. Conclusion

In this work we have carried out a detailed study about the effect of temperature and oxygen partial pressure on the O/T phase transition in $GdBaCo_2O_{5+\delta}$. The transition temperature shifts to lower values as the oxygen partial pressure decreases. The change of enthalpy associated to the O/T transition was determined by DSC to be ~4 J/g. The oxygen content varies, across the phase transition, from 5.44 to 5.46 in air and around 5.43–5.44 in Ar indicating the existences of narrow two-phase field. The presence of hysteresis, a narrow two-phase field, $\Delta H \neq 0$ and $\Delta V \neq 0$ at constant temperature led us to conclude that this structural order/disorder transition is of first order type. This was confirmed by HT-XRD at 440 °C varying pO$_2$, where the coexistence of two phases was detected.

The partial molar enthalpy h_{O_2} exhibits a linear dependence with $5 + \delta$ for both, tetragonal and orthorhombic phase, which is consistent with the presence of itinerant charge carriers in Co3d–O2p band.

The higher h_{O_2} absolute value for the O phase should be related to a higher interaction between defects which predominates over the

thermal energy leading to the ordering of the oxygen vacancies along the *a*-direction.

The partial molar entropy s_{O_2} shows a small dependence with $5 + \delta$ for both phases, although a great change of values from oxygen ordered (O), $s_{O_2} \approx -50$ J mol^{-1} K^{-1}, to oxygen disordered (T) phase, $s_{O_2} \approx +100$ J mol^{-1} K^{-1} is observed. This variation in s_{O_2} can be related to the diminution of the configurational entropy in the O phase. In the case of the tetragonal phase, the behavior of s_{O_2} can also be fitted taking into account delocalized charge carrier in the Co3d–O2p band.

The electrical conductivity shows a characteristic metallic behavior. This result is consistent with the presence of delocalized charge carriers as was predicted from thermodynamic analysis. The variation of the mobility μ_p^0 from 125 cm^2 V^{-1} s^{-1} K for tetragonal phase to 200 cm^2 V^{-1} s^{-1} K for orthorhombic, may be a consequence of the Co$-$O$-$Co bond shortening along *a*-direction across transition. In both case, the $\frac{\mu_p^0}{T}$ is characteristic of large polaron mechanism where the free charge carriers move slowly because they must drag their polarization cloud through the polar solid.

Acknowledgments

References

[1] F. Fauth, E. Suard, V. Caignaert, I. Mirebeau, Phys. Rev. B: Condens. Matter Mater. Phys. 66 (18) (2002) 1844211.
[2] Y. Moritomo, T. Akimoto, M. Takeo, A. Machida, E. Nishibori, M. Takata, M. Sakata, K. Ohoyama, A. Nakamura, Phys. Rev. B: Condens. Matter Mater. Phys. 61 (20) (2000) R13325.
[3] M. Respaud, C. Frontera, J.L. García-Muñoz, M.Á.G. Aranda, B. Raquet, J.M. Broto, H. Rakoto, M. Goiran, A. Llobet, J. Rodríguez-Carvajal, Phys. Rev. B: Condens. Matter Mater. Phys. 64 (21) (2001) 2144011.
[4] C. Frontera, J.L. Garcia Muñoz, A. LLobet, Ll. Mañosa, M.Á.G. Aranda, J. Solid State Chem. 171 (2003) 349.
[5] E. Suard, F. Fauth, V. Caignaert, I. Mirebeau, Phys. Rev. B: Condens. Matter Mater. Phys. 61 (18) (2000) R11871.
[6] A. Taskin, Y. Ando, Phys. Rev. Lett. 95 (2005) 176603.
[7] S. Streule, A. Podlesnyak, J. Mesot, M. Medarde, K. Conder, K. Pomjakushina, E. Mitberg, V.J. Kozhevnikov, Phys.: Condens. Matter 17 (2005) 3317.
[8] A. Tarancón, S. Skinner, R. Chater, F. Hernández-Ramírez, J. Kilner, J. Mater. Chem. 17 (2007) 3175.
[9] J.-H. Kim, L. Mogni, F. Prado, A. Caneiro, J.A. Alonso, A. Manthiram, J. Electrochem. Soc. 156 (12) (2009) B1376.
[10] K. Zhang, L. Ge, R. Ran, Z. Shao, Sh. Liu, Acta Mater. 56 (2008) 4876.
[11] J.-H. Kim, F. Prado, A. Manthiram, J. Electrochem. Soc. 155 (10) (2008) B1023.
[12] M.-B. Choi, S.Y. Jeon, J.S. Lee, H.J. Hwang, S.J. Song, J. Power Sources 195 (2010) 1059.
[13] Ch. Yang, X. Wu, Sh. Fang, W. Liu, Mater. Lett. 63 (2009) 1007.
[14] J.T.S. Irvine, A. Azad, J.H. Kim, J. Power Sources 196 (2011) 7333.
[15] S. Streule, A. Podlesnyak, E. Pomjakushina, K. Conder, D. Sheptyakov, M. Medarde, J. Physica B: Cond. Matter 378–380 (2006) 539.
[16] L. Lo Presti, M. Allieta, M. Scavini, P. Ghigna, L. Loconte, V. Scagnoli, M. Brunelli, Phys. Rev. B 84 (2011) 104107.
[17] J.C. Burley, J.F. Mitchell, S. Short, D. Miller, Y. Tang, J. Solid State Chem. 170 (2003) 339.
[18] A. Taskin, A. Lavrov, Y. Ando, Phys. Rev. B 71 (2005) 134414.
[19] A. Maignan, C. Martin, D. Pelloquin, N. Nguyen, B.J. Raveau, J. Solid State Chem. 142 (1999) 247.
[20] A. Taskin, A. Lavrov, Y. Ando, Appl. Phys. Lett. 86 (2005) 091910.
[21] A. Tarancón, D. Marrero-López, J. Peña-Martínez, J.C. Ruiz-Morales, P. Núñez, Solid State Ionics 179 (2008) 611.
[22] N. Li, Z. Lü, B. Wei, X. Huang, K. Chen, Y. Zhang, W. Su, J. Alloys Compd. 454 (2008) 274.
[23] N. Li, Z. Lü, B. Wei, X. Huang, Y. Zhang, W. Su, Ceram. Int. 38 (2) (2012) 2159.
[24] B. Wei, Z. Lü, D. Jia, X. Huang, Y. Zhang, W. Su, Int. J. Hydrogen Energy 35 (2010) 3775.
[25] J.H. Kim, A. Manthiram, J. Electrochem. Soc. 155 (2008) B385.
[26] A. Tarancón, A. Morata, G. Dezanneau, S. Skinner, J. Kilner, S. Estradé, F. Hernández Ramirez, F. Peiró, J.R. Morante, J. Power Sources 174 (2007) 255.
[27] S. Streule, A. Podlensyak, D. Sheptyakov, E. Pomjakushina, M. Stiangaciu, K. Conder, M. Medarde, M. Patrakeev, I. Leonidov, V. Kozhevnikov, J. Mesot, Phys. Rev. B 73 (2006) 94203.
[28] J. Rodríguez-Carvajal, Fullprof: A Program for Rietveld Refinement and Profile Matching Analysis of Complex Powder Diffraction Patterns, Laboratoire Léon Brillouin (CEA-CNRS), http://www.ill.eu/sites/fullprof/.
[29] A. Caneiro, P. Bavdaz, J. Fouletier, J.P. Abriata, Rev. Sci. Instrum. 53 (1982) 1072.
[30] Ch. Genzel, I. Denks, J. Gibmeier, M. Klaus, G. Wagener, Nucl. Inst. Methods Phys. Res. A 578 (2007) 23.
[31] I. Denks, Ch. Genzel, Nucl. Inst. Methods Phys. Res. B 262 (2007) 87.
[32] http://www.certif.com/spec.html.
[33] C. Frontera, A. Caneiro, A. Carrillo, J. Oró-Solé, J.L. García Muñoz, Chem. Mater. 17 (2005) 5439.
[34] W. Liu, C. Yang, X. Wu, H. Gao, Z. Chen, Solid State Ionics 192 (2011) 245.
[35] P.S. Anderson, C. Kirk, J. Knudsen, I.M. Reaney, A.R. West, Solid State Sci. 7 (2005) 1149.
[36] D.S. Tsevetkov, V.V. Sereda, A. Zuev, Solid State Ionics 180 (2010) 1620.
[37] E. Bucher, W. Sitte, G.B. Caraman, V.A. Cherepanov, T.V. Aksenova, M.V. Ananyev, Solid State Ionics 177 (2006) 3109.
[38] L. Mogni, F. Prado, A. Caneiro, Chem. Mater. 18 (17) (2006) 4163.
[39] L. Mogni, J. Fouletier, F. Prado, A. Caneiro, J. Solid State Chem. 178 (2005) 2715.
[40] N. Grunbaum, L. Mogni, F. Prado, A. Caneiro, J. Solid State Chem. 177 (2004) 2350.
[41] IUPAC, Commission on Thermodynamics; Oxygen—International Thermodynamics Tables of the Fluid State-9, Blackwell Sci, Oxford, 1987.
[42] M.H.R. Lankhorst, H.J. Bouwmeester, H. Verweij, J. Am. Ceram. Soc. 80 (1997) 2175.
[43] M.H.R. Lankhorst, H.J. Bouwmeester, H. Verweij, Phys. Rev. Lett. 77 (1996) 2989.
[44] M.H.R. Lankhorst, H.J. Bouwmeester, H. Verweij, J. Solid State Chem. 133 (1997) 555.
[45] P. Hjalmarsson, M. Søgaard, M. Mogensen, J. Solid State Chem. 183 (2010) 1853.
[46] D.S. Tsevetkov, V.V. Sereda, A.Y. Zuev, Solid State Ionics 192 (2011) 215.